

Geodetic Imaging of Time-Dependent Three-Component Surface Deformation: Application to Tidal-Timescale Ice Flow of Rutford Ice Stream, West Antarctica

Pietro Milillo, *Senior Member, IEEE*, Brent Minchew, Mark Simons, Piyush Agram, and Bryan Riel

Abstract—We present a method for inferring time-dependent three-component surface deformation fields given a set of geodetic images of displacements collected from multiple viewing geometries. Displacements are parameterized in time with a dictionary of displacement functions. The algorithm extends an earlier single-component (i.e., single line of sight) framework for time-series analysis to three spatial dimensions using combinations of multitemporal, multigeometry interferometric synthetic aperture radar (InSAR) and/or pixel offset (PO) maps. We demonstrate this method with a set of 101 pairs of azimuth and range PO maps generated for a portion of the Rutford Ice Stream, West Antarctica, derived from data collected by the COSMO-SkyMed satellite constellation. We compare our results with previously published InSAR mean velocity fields and selected GPS time series and show that our resulting three-component surface displacements resolve both secular motion and tidal variability.

Index Terms—3-D analysis, ocean tides, pixel offsets (POs), Rutford ice stream (RIS), synthetic aperture radar (SAR), time-series analysis.

I. INTRODUCTION

SYNTHETIC aperture radar (SAR) is a well-established remote sensing technique characterized by its day/night and all-weather acquisition capabilities, wide spatial coverage, and fine spatial resolution. The increasing availability of SAR-based geodetic measurements, including interferometric SAR (InSAR) and pixel offset (PO) maps, allows for a detailed

Manuscript received May 28, 2016; revised September 16, 2016, November 22, 2016, and May 3, 2017; accepted May 24, 2017. Date of publication June 29, 2017; date of current version September 25, 2017. The work of P. Milillo was supported by the National Aeronautics and Space Administration Postdoctoral Program. The work of B. Minchew was supported in part by NASA Cyospheric Sciences under Award NNX14AH80G, in part by National Science Foundation Earth Sciences Postdoctoral Fellowship under Award 1452587, and in part by Albert Parvin and ARCS LA Chapter Foundations. The work of B. Riel was supported by NASA Earth and Space Sciences Fellowship. (*Corresponding author: Pietro Milillo.*)

P. Milillo and P. Agram are with the Jet Propulsion Laboratory, California Institute of Technology, Pasadena, CA 91109 USA (e-mail: pietro.milillo@jpl.nasa.gov).

B. Minchew is with the Seismological Laboratory, California Institute of Technology, Pasadena, CA 91125 USA, and also with the British Antarctic Survey, Cambridge CB3 0ET, U.K.

M. Simons is with the Seismological Laboratory, California Institute of Technology, Pasadena, CA 91125 USA.

B. Riel is with the Jet Propulsion Laboratory, California Institute of Technology, Pasadena, CA 91109 USA, and also with the Seismological Laboratory, California Institute of Technology, Pasadena, CA 91125 USA.

Color versions of one or more of the figures in this paper are available online at <http://ieeexplore.ieee.org>.

Digital Object Identifier 10.1109/TGRS.2017.2709783

monitoring of ground deformation associated with various geophysical and anthropogenic phenomena [1], [2]. In comparison with InSAR line-of-sight phase-based measurements, PO techniques are characterized by lower sensitivity and coarser resolution, with the achievable resolution and sensitivity roughly dependent on the size of the adopted correlation window and the resolution of the SAR data (see [3]).

Several techniques have been developed for combining SAR observations collected along a single-line of sight (LOS) direction into deformation time series (see [4]–[7]). These techniques are often used to study the phenomena that have slow deformation rates relative to the repeat time of the SAR observations. But constellations of satellites with a short repeat time, such as COSMO-SkyMed (CSK), Sentinel-1A/B, and TerraSAR-X/PAZ systems, allow for improved temporal resolution and expanded applicability of time-series approaches. In some cases, these capabilities allow for the extension of single-LOS methods to two or three components of the deformation field.

In order to reconstruct the complete three-component vectors, several approaches merge combinations of data sets from multiple viewing geometries. Many of these techniques reduce the effective dimensions of the estimation problem by making assumptions such as a negligible north–south component of deformation (see [8], [9]), surface parallel motion [10]–[12], and/or constant displacement rates during different acquisitions (see [13]–[18]). In some cases, it may be useful to assume a single step-function displacement (e.g., for earthquakes) or, alternatively, a constant velocity (e.g., for quasi-secular ice flow or interseismic crustal deformation), which effectively removes temporal variability and reduces the problem to a simple reconstruction of a single set of east, north, and up components for every pixel (see [19]–[25]). For other applications, it is adequate to define a common temporal sampling between ascending and descending passes, assuming negligible relative deformation between their acquisition times [26] or alternatively, minimize differences in inferred velocity between consecutive acquisition periods [27].

In this study, we focus on a method for inferring time-dependent three-component motion of the surface associated with the modulation of ice-stream/ice-shelf motion driven by ocean tides. In particular, we use CSK acquisitions spanning

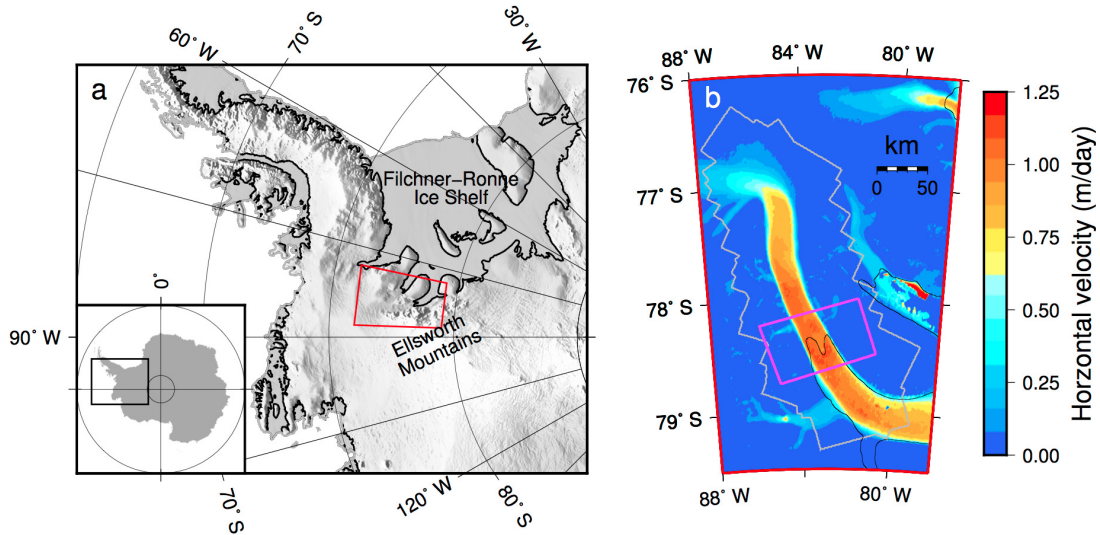


Fig. 1. Location of CSK InSAR data collected from August–September 2013. (a) Shaded relief map of a portion of the west Antarctica and the Antarctic Peninsula; red outline shows the extent of (b). (b) Horizontal velocity field from [12]. Purple outline shows the spatial extent of the region of interest considered in this study. Gray outline indicates the extent of CSK coverage, and the black line indicates an estimate of the grounding line [28].

9 months, beginning in August 2013, for estimating surface velocities and tidal variations over Rutford Ice Stream (RIS), West Antarctica (Fig. 1). RIS is known to experience significant tidally induced flow variations at different frequencies. Here, we invert for a set of tidal constituents previously identified using GPS observations [29], [30]. This procedure allows us to quantify spatial and temporal variations associated with tidal forcing in the vicinity of the ice-stream grounding line, and the boundary between the grounded ice stream and floating ice shelf. The inferred time series, combined with physical modeling, can eventually improve our basic understanding of the evolution of glaciers and ice sheets and address several key questions related to mechanisms that influence basal sliding and how stresses are transmitted over long distances upstream of the grounding line [30]–[32].

The discussion is organized as follows. Section II describes the methodology and algorithms focusing on the PO and the three-component surface velocity field estimation together with the associated sensitivity and error analysis. Section III presents the data set and the model optimization. Section IV describes the results and comparisons with independent GPS and InSAR data sets. Section V describes the potential for our technique to improve the understanding of the evolution of glaciers and large ice masses.

II. METHODS AND ALGORITHMS

In this section, we describe the methods behind the three-component displacement time-series estimation algorithm. We first describe the PO displacement observations and then formulate the time-series estimation problem. We then introduce the geometric equations used to derive the 3-D displacement field.

A. Pixel Offset Estimates

Amplitude image tracking, also known as speckle tracking, uses the magnitude (or intensity) for cross correlation of the

corresponding image. We select small subsets of master and slave images and estimate the displacement in LOS and along-track (AT) directions that results in the maximum cross correlation (see [34]). The complex single look complex images are resampled by a factor of 2 in both range and azimuth to refine estimates of the correlation surface. The PO measurements are resolvable to within 5% and 10% of the image pixel size [3], [34], [35]. The pixel size is about 2.5 m in both azimuth and range for the CSK X-band Stripmap-HIMAGE products. We used cross-correlation windows with the dimensions of 64×64 pixels, and estimated offsets every 32 pixels in both range and azimuth direction.

Single-look complex SAR images were produced using the JPL/Caltech InSAR Scientific Computing Environment [36]. We use the Bedmap2 digital elevation model [37], resampled to 25-m grid spacing using bicubic interpolation, to calculate and remove topographic effects, as well as for geocoding the final PO maps. In the descending SAR geometry, ice motion is mainly recorded in the range PO (RPO), while the azimuth PO (APO) shows more deformation in the ascending acquisitions (Fig. 2). In the ascending acquisitions, the horizontal component of ice-stream motion is nearly parallel to the look direction of the CSK satellites and is shown as positive motion.

In some cases, we removed residual orbital ramps before the three-component inversion, masking out regions with large motions to minimize bias and fitting a quadratic polynomial to the offsets. PO measurements from pairs with large perpendicular baselines have topographic residuals across the ice stream. Digital elevation model (DEM) flattening has also been applied before the 3-D processing for the RPO.

For some days, PO maps show a nonzero vertical component of motion at the grounding zone of the ice stream (Fig. 2), indicating periodic variability to the floating ice deformation. Over longer time intervals, the ice stream moves many meters and even PO measurements may not be possible because of changes in backscatter properties of the ice-stream surface.

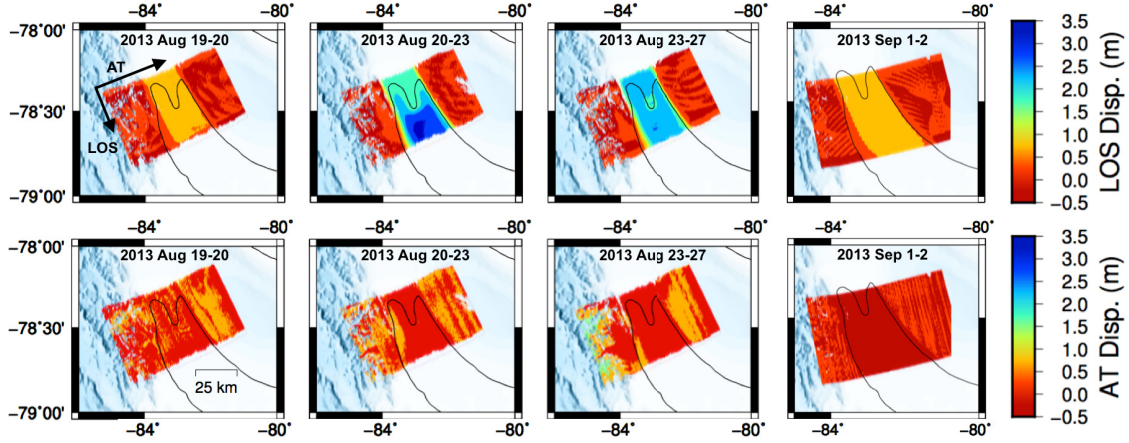


Fig. 2. Range and azimuth PO formed with scenes acquired on the indicated dates. The southern half of the ice stream in these scenes is floating as part of the Ronne Ice Shelf, and the large difference in LOS displacement is due primarily to induced tidal motions. Positive values indicate deformation toward the sensor (RPO) and the flight direction (APO).

For RIS imaged with CSK, we find RPO and APO estimates are not routinely possible when images are separated by more than 8 days.

B. (*e, n, u*) Domain

We consider an acquisition plan of N unique SAR scenes acquired from ascending and descending orbits at times $(t_1 \dots t_N)$. We combine these SAR scenes into M total displacement maps, designated Λ , over a total study period of time τ .

In general, three-component displacements of the surface can be described as the sum of a secular velocity plus time-dependent periodic and transient terms. Our interest in this study is to capture tidal variability on RIS, which can be described as set of sinusoids [29], [30]; thus, we consider only a secular velocity augmented by a set of k sinusoidal functions. The instantaneous three-component surface displacement at any given geographic position is defined as

$$\delta(t_i) = \mathbf{v}t_i + \sum_{p=1}^k \mathbf{f}_p(t_i) \quad (1)$$

where $\mathbf{v} = [v^e \ v^n \ v^u]^T$ is the secular velocity vector (in meters/year), t_i is the time, in years, elapsed since the first acquisition in the data set, and \mathbf{f}_p is the three-component sinusoidal vector defined as

$$\mathbf{f}_p(t) = \begin{bmatrix} a_p^e \sin(\omega_p t + \phi_p^e) \\ a_p^n \sin(\omega_p t + \phi_p^n) \\ a_p^u \sin(\omega_p t + \phi_p^u) \end{bmatrix} \quad (2)$$

where a_p^{ζ} is the amplitude and ϕ_p^{ζ} is the phase for angular frequency ω_p along spatial coordinate ζ .

InSAR and PO techniques provide measurements of component of the displacement projected onto an observational unit vector $\hat{\mathbf{l}}$ over finite-time interval. Considering (1) and (2), we can write a single-component displacement map over timespan $\Delta t_{ij} = t_j - t_i$ as

$$\Lambda_{i,j} = \psi_{i,j} \hat{\mathbf{l}} \cdot \left(\mathbf{v} \Delta t_{ij} + \sum_{p=1}^k [\mathbf{f}_p(t_j) - \mathbf{f}_p(t_i)] \right) \quad (3)$$

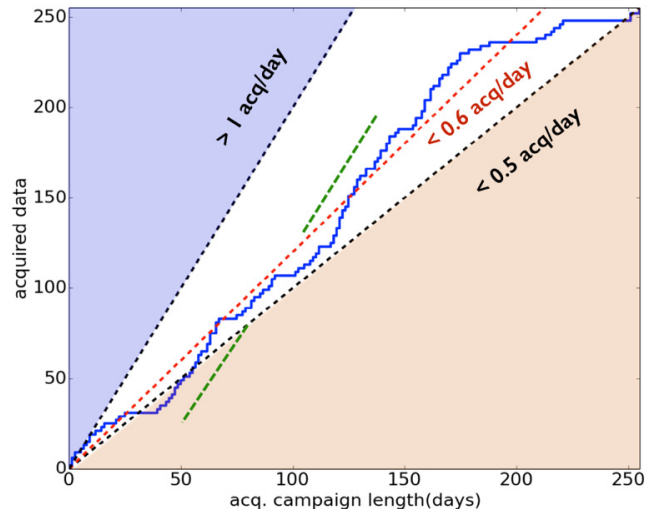


Fig. 3. Cumulative number of image acquisitions over RIS during the period of the campaign. Every acquisition is used as part of a pair for estimating range and azimuth POs.

where the incidence-like matrix (commonly called the design matrix in graph theory and referred to as \mathbf{A} in Small BAseLine Subset terminology [5]) is given as

$$\psi_{i,j} = \begin{cases} 1 \forall i > j \wedge \Lambda_{i,j} \in \mathbf{d} \\ -1 \forall i < j \wedge \Lambda_{i,j} \in \mathbf{d} \\ 0 \text{ elsewhere} \end{cases} \quad (4)$$

where \mathbf{d} is an $M \times 1$ vector containing the PO maps. Later, we will employ a least-squares inversion to derive the best-fit, time-dependent, three-component velocity model to the observations. We rewrite (3) as

$$\Lambda_{i,j} = \psi_{i,j} \hat{\mathbf{l}} \cdot \left(\mathbf{v} \Delta t_{ij} + \sum_{p=1}^k [s_p(t_j) - s_p(t_i)] + \mathbf{c}_p(t_j) - \mathbf{c}_p(t_i) \right) \quad (5)$$

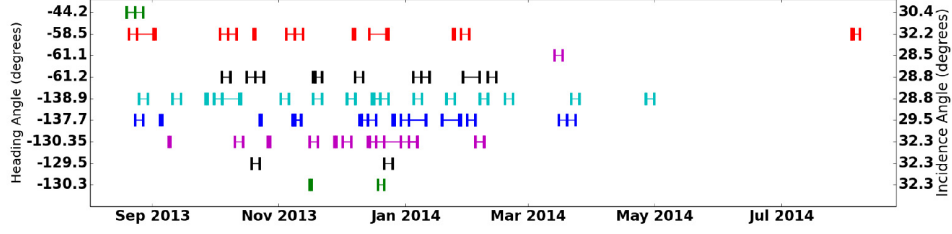


Fig. 4. Temporal distribution of the multi-LOS used in this study. Each color corresponds to different tracks with different headings. The Italian Space Agency controlled experiment was run maintaining baselines within an orbital tube of approximately 150 m. The horizontal segments represent the used InSAR pairs. Some vertical segments may appear thicker than others due to the 1-day pair acquisitions.

where

$$s_p(t_\zeta) = \begin{bmatrix} A_p^e \\ A_p^n \\ A_p^u \end{bmatrix} \sin(\omega_p t_\zeta) \quad (6)$$

$$c_p(t_\zeta) = \begin{bmatrix} B_p^e \\ B_p^n \\ B_p^u \end{bmatrix} \cos(\omega_p t_\zeta). \quad (7)$$

After inferring the unknown values A_p^ζ and B_p^ζ for each sinusoid p along spatial coordinate $\zeta = [e, n, u]$ using the method described later, we can retrieve the amplitude and phase values defined in (2) by noting that

$$a_p^\zeta = \sqrt{(A_p^\zeta)^2 + (B_p^\zeta)^2} \quad (8)$$

$$\phi_p^\zeta = \tan^{-1}(B_p^\zeta/A_p^\zeta). \quad (9)$$

Given the model for surface displacements in (5), we can solve the least-squares problem for each pixel which minimizes the cost function Γ

$$\Gamma = \|\Psi \cdot (\mathbf{L} \circ \mathbf{P}) \cdot \mathbf{m} - \mathbf{d}\|_2^2 \quad (10)$$

where Ψ is the $M \times 2N$ matrix containing the $\psi_{i,j}$ values. \mathbf{P} and \mathbf{L} are the $2N \times (6k + 3)$ matrices, \mathbf{P} contains the parameter functions (sinusoidal and linear terms) evaluated at the acquisition time t_i , and \mathbf{L} contains the unit vectors $\hat{\mathbf{l}}$ projecting the LOS and AT displacement into the east, north, and up directions. The vector \mathbf{m} contains the $6k + 3$ parameters to be estimated. The operator \circ represents the Hadamard product, while the \cdot operator is the Kronecker product (see the Appendix for details on \mathbf{L} , \mathbf{P} , and \mathbf{m}). To simplify the description of our formulation, we assumed that both LOS and AT displacement maps are available at every time t_i . However, this formulation can accommodate a general set of LOS and AT displacements.

C. Error Analysis, Model Resolution Matrix, and Dilution of Precision

The errors on the model parameters are sensitive to the details of the temporal sampling, the variety of imaging geometries, the error of each observation, and the number of modeled parameters. Assuming a given set of acquisitions and a dictionary of user-chosen temporal functions, we can estimate the number of optimal parameters and their errors. Assuming independent, normally distributed random errors,

the covariance of the estimated parameters can be written as

$$\mathbf{C}_m = \sigma_d \mathbf{I} [\mathbf{G}^T \mathbf{G}]^{-1} \quad (11)$$

where

$$\mathbf{G} = \Psi \cdot \mathbf{L} \quad (12)$$

and the data covariance matrix \mathbf{C}_d is assumed to be the identity matrix with $\sigma_d = 1$ (i.e., unweighted least squares). A useful dimensionless metric encapsulating how the satellite viewing configuration will affect the accuracy of the deformation field is the geometrical dilution of precision (GDOP). GDOP is widely used in GPS analysis and also recently used with InSAR airborne data [18]. We use a similar quantity provided by the cumulative GDOP for understanding how well our three-component displacement field can be resolved given a certain set of SAR displacement fields. We write

$$\text{GDOP} = \sqrt{\text{tr}(\mathbf{C}_m)} \quad (13)$$

where $\text{tr}()$ is the trace operator. GDOP can be used as an estimate of the expected accuracy averaged across all components.

In order to estimate the maximum number of resolvable parameters given our actual acquisition plan, we calculate the determinant of $\mathbf{G}^T \mathbf{G}$ and make sure that it is nonzero (full rank).

III. DATA SET

Our data set consists of six stacks of CSK-stripmap Himage H4 [38] data acquired starting in 2013 when ASI was undertaking a controlled baseline experiment for the interferometric CSK Tandem mission. We processed a total of 101 SAR pairs collected along nine satellite tracks, in both ascending and descending orbital directions. All data were collected with HH (horizontal transmit and receive) polarization and in right-look configurations generating both azimuth and range offsets. See Fig. 3 for more details. The acquisitions were planned to maximize temporal and spatial coverage. We selected a subset of 21 one-day pairs, 30 three-day pairs, 24 four-day pairs, and 26 eight-day pairs (Fig. 4). The selected data typically have perpendicular baselines shorter than 200 m, with many baselines shorter than 100 m, and high signal-to-noise ratios in the areas of interest.

A. Model Parameters Optimization

Before considering the real observations, we first generated a synthetic data set of three-component surface displacements

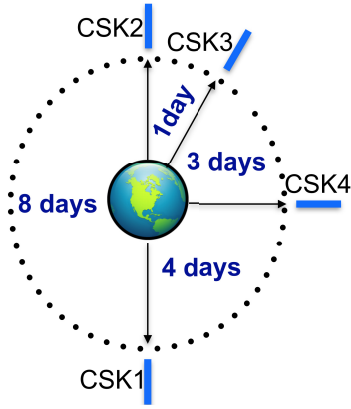


Fig. 5. Relative position of the four satellites in the CSK constellation in the orbital plane and repeat time in the interferometric mode (adapted from [33]).

subject to tidal oscillations at periods consistent with those inferred from the power spectra of available GPS time series [28], [29] (see auxiliary material Table I). We sample the synthetic data consistent with the actual temporal sampling of our suite of observations (Fig. 4).

We considered several tests, including assuming different sets of tidal periods, in order to guide our selection of which periods to include in the final inversion. For details on synthetic tests, we refer the reader to the supplementary material in [39]. Because our observation period is relatively short (9 months), we exclude the semiannual S_{sa} and the annual S_a solar constituents. We also limit the set of tides to those not aliased by the CSK repeat acquisition sampling (exact multiples of the repeat time, e.g., S_2 , K_2 , P_1 , and K_1). The remaining tides are the lunar monthly M_m , the luni-solar synodic fortnightly M_{sf} , the luni-solar fortnightly M_f , the diurnal O_1 , and the lunar semidiurnal M_2 constituents.

Fig. 5 shows the acquisition rate over the grounding line. We have an average acquisition rate of 0.6 acquisition/day with a maximum of 1 acquisition/day. There are also time intervals with little coverage between October and December of 2013 and March and May–June of 2014 (Figs. 4 and 5).

We are also limited in our ability to reconstruct several tidal periods due to the low signal-to-noise ratio. The CSK-stripmap PO sensitivity excludes the possibility of reconstructing the M_m and M_f tides for both the vertical and the horizontal and the O_1 and M_2 tides for the horizontal amplitude.

We chose a set of functions for the three-component time-series inversion that provides the best tradeoff between the principal tides affecting Rutford (see auxiliary material Table I), the tidal periods that are resolvable with the available CSK acquisitions and the SNR characterizing the PO maps. Surface velocities on RIS vary by approximately 20% over 14.77-day periods as a result of the tidal forcing [29], [30], [39]. The power is approximately evenly distributed between the M_{sf} fortnightly (14.77 period) and the K_2 luni-solar and S_2 solar semidiurnal tides [29], [30].

TABLE I
MOST IMPORTANT TIDAL CONSTITUENTS RELEVANT TO THE RIS AREA FROM [30]

Tide	Period (days)	Horiz. Amp (m)	Horiz. Phase (deg)	Vert. Amp. (m)	Vert. Phase (deg)
Sa	365.27	0.1918	273	0.002	179
Ssa	182.62	0.2674	256	0.015	179
Mm	27.55	0.0504	253	0.016	63
MSf	14.77	0.1328	18.8	0.003	164
Mf	13.66	0.0254	250	0.029	163
O1	1.08	0.0026	81	0.43	54
P1	1.003	0.0024	77	0.166	64
K1	1	0.0019	79	0.49	73
M2	0.52	0.0026	177	1.563	70
S2	0.5	0.0036	184	1.016	115
K2	0.498	0.031	163	0.291	99

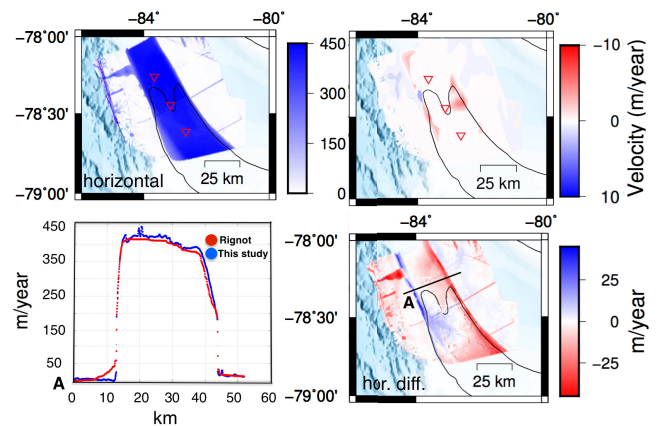


Fig. 6. (Top left) Horizontal and (Top right) vertical 3-D secular displacements near the RIS grounding line. (Bottom right) Horizontal velocity differences calculated using horizontal displacement fields from [11]. (Bottom left) Cross section. Grounding line position from [28]. Red and white triangles represent the GPS position from [29].

In our case, we only included the M_{sf} tide for the horizontal component and the O_1 and M_2 tidal constituents for the vertical component. The M_{sf} vertical component is negligible compared to the O_1 and M_2 . Tidal and secular displacements give generally better results over grounded ice than floating ice. We are able to reproduce within 7% and 15% the synthetic horizontal and vertical velocity fields, respectively, within formal error. Our tests suggest that when M_2 vertical component is not included in the inversion, secular velocity inferred vertical components differ by one-third when compared to the synthetic signal over the floating ice. When M_2 and O_1 verticals are included in the inversion, velocities are well within 4% of the actual velocity. We recover horizontal tidal signal within 90% of the synthetic signal. Based on our synthetic tests and the CSK acquisition sampling, our

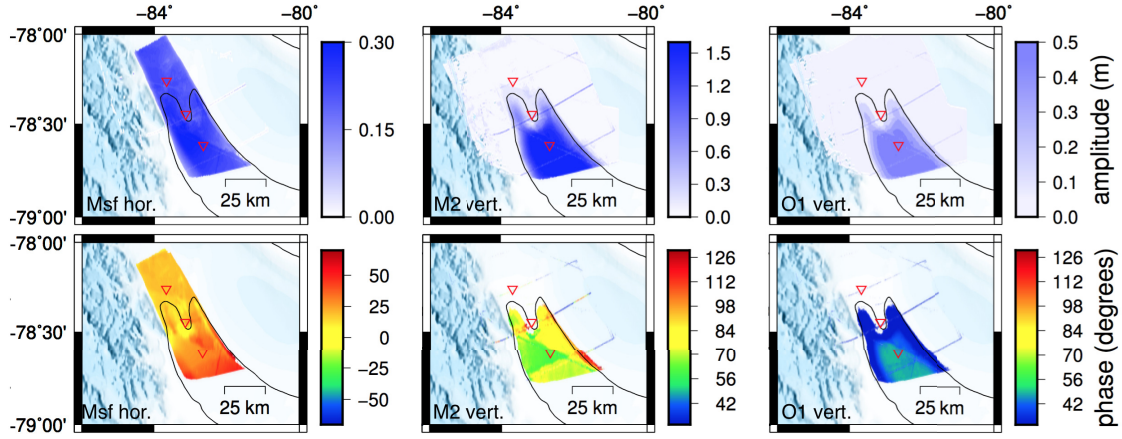


Fig. 7. Tidal components over the Rutford ice-stream grounding line. Grounding line position from [24]. Red and white triangles represent the GPS position from [29]. (Top left) M_{sf} (14.77 days) amplitude. (Bottom left) M_{sf} (14.77 days) phase. (Top center) M_2 (0.52 day) amplitude. (Bottom center) M_2 (0.52 day) phase. (Top right) O_1 (1.08 days) amplitude. (Bottom right) O_1 (1.08 days) amplitude.

dictionary of functions is

$$d_e(t_i) = v_e t_i + A_{M_{sf}}^e \sin(\omega_{M_{sf}} t_i) + B_{M_{sf}}^e \cos(\omega_{M_{sf}} t_i) \quad (14)$$

$$d_n(t_i) = v_n t_i + A_{M_{sf}}^n \sin(\omega_{M_{sf}} t_i) + B_{M_{sf}}^n \cos(\omega_{M_{sf}} t_i) \quad (15)$$

$$d_u(t_i) = v_u t_i + A_{O_1}^u \sin(\omega_{O_1} t_i) + B_{O_1}^u \cos(\omega_{O_1} t_i) \\ + A_{M_2}^u \sin(\omega_{M_2} t_i) + B_{M_2}^u \cos(\omega_{M_2} t_i). \quad (16)$$

Inspection of the model resolution matrix indicates that the final set of tidal periods chosen is well-resolved given the available set of interferograms.

IV. RESULTS

A. Velocity Fields

Our final estimated three-component surface velocity and tidal components are shown in Figs. 6 and 7. The RIS grounding zone is clearly visible in the vertical component of the O_1 and M_2 (periods of 1.08 and 0.52 days, respectively) tides, while the M_{sf} horizontal component does not show this feature and extends several kilometers upstream of the grounding line. The shear margins are very distinct in the three-component velocity estimates. Negative vertical velocities indicate thinning (Fig. 6).

Horizontal (north and east combined components) speed in the CSK data varies from 290 m/yr upstream to 430 m/yr toward the grounding line. Standard deviations of the velocities vary around 10%–20% of the observed values. We compared our velocity results with earlier InSAR estimates [12], finding an average difference of 25–30 m/yr over RIS (~10% of the total displacement). Comparison of our horizontal velocity field with that from [12] (Fig. 6) shows the largest differences at the ice-stream margins, suggesting a nonnegligible difference in the inferred shear margin velocity. This difference is presumably due to the different ground resolutions of the different estimates. The pixel size of the CSK-derived offsets is approximately 45 m, while results from [12] have a ground resolution of about 450 m. Smoothing and interpolation of the fields in [12] may also play a role.

Vertical velocity is approximately zero (Fig. 6) over the observed area, consistent with the shallow DEM slope. Close

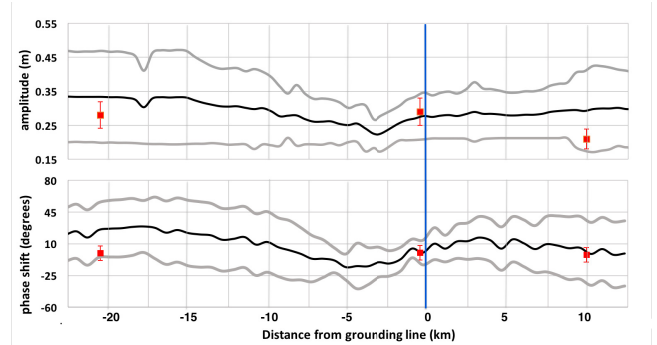


Fig. 8. GPS (squares) and CSK (lines) in-line amplitude and phase M_{sf} tide measurement. The graph has been adapted from [29]. Gray error bars show two sigma values estimated from the proposed algorithm.

to the east shear margin, we observe upstream thickening and downstream thinning with maximum magnitudes of 7 m/yr. The vertical motion is characterized by a larger uncertainty as compared to horizontal velocities. We found that the standard deviation is approximately equal to the observed velocity field. This effect is expected since only half of the data set (RPO) is sensitive to vertical displacements.

B. Tidal Signal

Our primary result is demonstrating the possibility of monitoring the ice-flow variation due to tidal forcing of the ice shelf and the grounding zone. Previous studies [28], [29] report the lunar semidiurnal M_2 (0.52 day) and the solar semidiurnal S_2 (0.50 day) as dominant vertical tidal constituents for the ice stream. The dominant horizontal ice along-flow variability is 14.77 days, i.e., the spring-neap M_{sf} tide [28], [29], [40]. The spring-neap tides occur twice during each lunar month and are due to interference of $M_2 + S_2$ semidiurnal tides. We compared the horizontal amplitude and phase obtained with SAR data with GPS data (shown in [28]). Results of tidal signal and GPS comparison are shown in Figs. 7 and 8, respectively. The amplitude and phase of the along-flow M_{sf} period motion are consistent with GPS observations (Fig. 8),

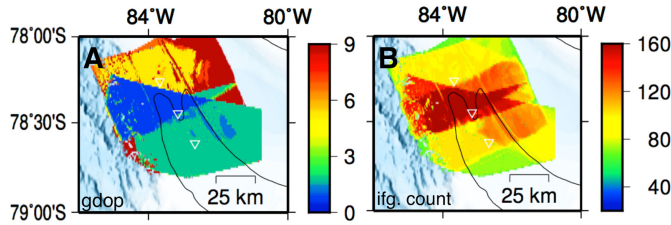


Fig. 9. (A) Geometrical dilution of position. (B) Number of displacement maps used for each pixel.

confirming along-flow upstream propagation modulating the RIS horizontal velocity.

We estimate a maximum amplitude of 0.4 and 1.6 m for the vertical component of the O_1 and M_2 tides, respectively. The inferred vertical M_2 and O_1 tides' amplitudes are consistent with existing GPS measurements [28], [29] (see the Appendix and Table I).

Phase measurements (Fig. 7, M_2 vertical) show phase jumps of about 8° with a standard deviation of 12° that appear to not have a physical meaning when interpreting deformation at RIS. We observe that phase jumps occur between different CSK acquisition frames. We interpret this phase shift as the result of an increased GDOP (Fig. 9) that limits the accuracy of the inferred results. Small amplitude values also lead to a poor constraint of the phase.

V. CONCLUSION

We describe the construction of time series of three-component surface displacements that resolve both secular motions and tidal variability from multitemporal, multigeometry SAR image POs. Flow-line parallel displacements at M_{sf} periods obtained with SAR data are consistent with sparse GPS observations [29]. Near the grounding line of RIS, M_{sf} displacements are typically up to 10% of the horizontal velocities. These results are consistent with previous GPS measurements [29], [30]. Comparisons with previous InSAR measurements show an approximately 5% difference in the horizontal velocity over the ice stream, and we attribute this discrepancy to the smoothing imposed and to the larger pixel size of the output map used in [12]. O_1 and M_2 vertical- and M_{sf} horizontal-inferred tides match with the GPS data although jumps occur in the SAR phase estimate of the O_1 and M_2 tides due to reduced GDOP values. M_{sf} along-flow upstream propagation inferred by SAR-based measurements agrees with GPS measurements [28], [29], confirming that RIS horizontal velocity is modulated by the M_{sf} spring-neap tide.

In this study, we capitalize on information coming from SAR measurements, which are able to provide coverage of ground deformation at spatial scales not reasonably accessible with *in situ* measurements such as GPS. Starting from a tidal spectrum calculated using GPS measurements, we exploited the space-borne SAR ability of acquiring data in remote areas, such as Antarctica, where *in situ* geodetic campaigns are logistically challenging and optical sensors may be ineffective due to darkness or atmospheric conditions. We used the

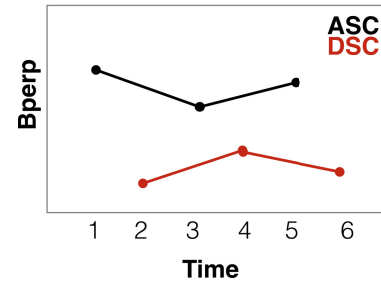


Fig. 10. Baseline plot for ASC and DSC data set. Each connection includes RPO and APO.

unique characteristics of the CSK constellation to acquire data in interferometric mode with unprecedented short revisit time as well as the high spatial resolution (~ 3 m) of the X-band sensor satellites, to resolve a set of tides not aliased by the constellation repeat time. We were able to reconstruct the M_{sf} spring-neap horizontal tide and the diurnal O_1 and the semidiurnal M_2 vertical tidal constituents. Due to decreasing repeat acquisition intervals and reduced latency in data availability, SAR techniques are now beginning to provide effective short-term monitoring that, together with recently developed techniques and their utilization, will improve the understanding of the evolution of glaciers and large ice sheets.

APPENDIX

In this section, we provide further details of the matrix formulation adopted herein. Given θ and φ as the heading and incidence angles, respectively, we explicitly define \mathbf{L} , \mathbf{P} , and \mathbf{m} in (17)–(21), as shown at the bottom of page 8. It is important to notice that the observational unit vector $\hat{\mathbf{l}}$ depends on the acquisition time since several interferometric stacks are utilized in the inversion.

We show how to construct for a small set of acquisitions the over-determined system of equations in (10). We assume to have six acquisitions equally divided between one ASC and one DSC track. Ascending and descending acquisitions are subsequent in time. We generate PO maps (ASC and DSC) according to the graph in Fig. 10. For the sake of simplicity, we hypothesize that our dictionary of functions is composed by a linear term and one sinusoidal function. These are general assumptions used only for simplifying the notation. Our system of equations is represented in (22)–(24), as shown at the bottom of page 8, and (25) and (26), as shown at the top of page 9.

ACKNOWLEDGMENT

The authors would like to thank H. Gudmundsson, P. Lundgren, and H. Martens, for their beneficial conversations. They used the original COSMO-SkyMed product (copyright ASI—Agenzia Spaziale Italiana, 2013–2016). COSMO-SkyMed data products are processed at JPL under license from ASI as part of a collaborative project between CIDOT and JPL/Caltech. The authors would like to thank

the Advanced Rapid Imaging Analysis system for facilitating data organization. The cost function Γ has been minimized using the Numpy linalg solver. The authors would also like to thank two anonymous reviewers for their com-

$$\mathbf{L} = \begin{pmatrix} l^e(t_1, \theta, \varphi) & l^n(t_1, \theta, \varphi) & \cdots & l^e(t_N, \theta, \varphi) & l^n(t_N, \theta, \varphi) \\ l^u(t_1, \theta, \varphi) & l^u(t_1, \theta, \varphi) & \cdots & l^u(t_N, \theta, \varphi) & l^u(t_N, \theta, \varphi) \\ l^e(t_1, \theta, \varphi) & l^n(t_1, \theta, \varphi) & \cdots & l^e(t_N, \theta, \varphi) & l^n(t_N, \theta, \varphi) \\ l^u(t_1, \theta, \varphi) & l^u(t_1, \theta, \varphi) & \cdots & l^u(t_N, \theta, \varphi) & l^u(t_N, \theta, \varphi) \\ \vdots & \vdots & \ddots & \vdots & \vdots \\ l^e(t_1, \theta, \varphi) & l^n(t_1, \theta, \varphi) & \cdots & l^e(t_N, \theta, \varphi) & l^n(t_N, \theta, \varphi) \\ l^u(t_1, \theta, \varphi) & l^u(t_1, \theta, \varphi) & \cdots & l^u(t_N, \theta, \varphi) & l^u(t_N, \theta, \varphi) \\ l^e(t_1, \theta, \varphi) & l^n(t_1, \theta, \varphi) & \cdots & l^e(t_N, \theta, \varphi) & l^n(t_N, \theta, \varphi) \\ l^u(t_1, \theta, \varphi) & l^u(t_1, \theta, \varphi) & \cdots & l^u(t_N, \theta, \varphi) & l^u(t_N, \theta, \varphi) \\ l^e(t_1, \theta, \varphi) & l^n(t_1, \theta, \varphi) & \cdots & l^e(t_N, \theta, \varphi) & l^n(t_N, \theta, \varphi) \\ l^u(t_1, \theta, \varphi) & l^u(t_1, \theta, \varphi) & \cdots & l^u(t_N, \theta, \varphi) & l^u(t_N, \theta, \varphi) \\ l^e(t_1, \theta, \varphi) & l^n(t_1, \theta, \varphi) & \cdots & l^e(t_N, \theta, \varphi) & l^n(t_N, \theta, \varphi) \\ l^u(t_1, \theta, \varphi) & l^u(t_1, \theta, \varphi) & \cdots & l^u(t_N, \theta, \varphi) & l^u(t_N, \theta, \varphi) \end{pmatrix} \quad (17)$$

$$\mathbf{P} = \begin{pmatrix} \sin(\omega_1 t_1) & \sin(\omega_1 t_1) & \cdots & \sin(\omega_1 t_N) & \sin(\omega_1 t_N) \\ \sin(\omega_1 t_1) & \sin(\omega_1 t_1) & \cdots & \sin(\omega_1 t_N) & \sin(\omega_1 t_N) \\ \sin(\omega_1 t_1) & \sin(\omega_1 t_1) & \cdots & \sin(\omega_1 t_N) & \sin(\omega_1 t_N) \\ \cos(\omega_1 t_1) & \cos(\omega_1 t_1) & \cdots & \cos(\omega_1 t_N) & \cos(\omega_1 t_N) \\ \cos(\omega_1 t_1) & \cos(\omega_1 t_1) & \cdots & \cos(\omega_1 t_N) & \cos(\omega_1 t_N) \\ \cos(\omega_1 t_1) & \cos(\omega_1 t_1) & \cdots & \cos(\omega_1 t_N) & \cos(\omega_1 t_N) \\ \vdots & \vdots & \ddots & \vdots & \vdots \\ \sin(\omega_k t_1) & \sin(\omega_k t_1) & \cdots & \sin(\omega_k t_N) & \sin(\omega_k t_N) \\ \sin(\omega_k t_1) & \sin(\omega_k t_1) & \cdots & \sin(\omega_k t_N) & \sin(\omega_k t_N) \\ \sin(\omega_k t_1) & \sin(\omega_k t_1) & \cdots & \sin(\omega_k t_N) & \sin(\omega_k t_N) \\ \cos(\omega_k t_1) & \cos(\omega_k t_1) & \cdots & \cos(\omega_k t_N) & \cos(\omega_k t_N) \\ \cos(\omega_k t_1) & \cos(\omega_k t_1) & \cdots & \cos(\omega_k t_N) & \cos(\omega_k t_N) \\ \cos(\omega_k t_1) & \cos(\omega_k t_1) & \cdots & \cos(\omega_k t_N) & \cos(\omega_k t_N) \\ \frac{t_1}{\tau} & \frac{t_1}{\tau} & \cdots & \frac{t_N}{\tau} & \frac{t_N}{\tau} \\ \frac{\tau}{t_1} & \frac{\tau}{t_1} & \cdots & \frac{\tau}{t_N} & \frac{\tau}{t_N} \\ \frac{\tau}{t_1} & \frac{\tau}{t_1} & \cdots & \frac{\tau}{t_N} & \frac{\tau}{t_N} \\ \tau & \tau & \cdots & \tau & \tau \end{pmatrix} \quad (18)$$

$$\mathbf{m} = [A_1^e \ A_1^n \ A_1^u \ B_1^e \ B_1^n \ B_1^u \ \cdots \ A_k^e \ A_k^n \ A_k^u \ B_k^e \ B_k^n \ B_k^u \ v^e \ v^n \ v^u] \quad (19)$$

$$\mathbf{I}(t_i, \theta, \varphi) = [l^e(t_i, \theta, \varphi) \ l^n(t_i, \theta, \varphi) \ l^u(t_i, \theta, \varphi)] = [-\sin(\varphi_{t_i}) \cos(\theta_{t_i}) \ \sin(\varphi_{t_i}) \ \sin(\theta_{t_i}) \ \cos(\theta_{t_i})] \text{ for RPO} \quad (20)$$

$$\mathbf{I}(t_i, \theta) = [l^e(t_i, \theta) \ l^n(t_i, \theta) \ l^u(t_i, \theta)] = [\sin(\theta_{t_i}) \ \cos(\theta_{t_i}) \ \mathbf{0}] \text{ for APO} \quad (21)$$

$$\mathbf{d} = (\Lambda_{13}^{RG} \ \Lambda_{13}^{AT} \ \Lambda_{24}^{RG} \ \Lambda_{24}^{AT} \ \Lambda_{35}^{RG} \ \Lambda_{35}^{AT} \ \Lambda_{46}^{RG} \ \Lambda_{46}^{AT}) \quad (22)$$

$$\mathbf{m} = [A_1^e \ A_1^n \ A_1^u \ B_1^e \ B_1^n \ B_1^u \ v^e \ v^n \ v^u] \quad (23)$$

$$\mathbf{P} = \begin{pmatrix} \sin(\omega_1 t_1) & \sin(\omega_1 t_1) & \cdots & \sin(\omega_1 t_6) & \sin(\omega_1 t_6) \\ \sin(\omega_1 t_1) & \sin(\omega_1 t_1) & \cdots & \sin(\omega_1 t_6) & \sin(\omega_1 t_6) \\ \sin(\omega_1 t_1) & \sin(\omega_1 t_1) & \cdots & \sin(\omega_1 t_6) & \sin(\omega_1 t_6) \\ \cos(\omega_1 t_1) & \cos(\omega_1 t_1) & \cdots & \cos(\omega_1 t_6) & \cos(\omega_1 t_6) \\ \cos(\omega_1 t_1) & \cos(\omega_1 t_1) & \cdots & \cos(\omega_1 t_6) & \cos(\omega_1 t_6) \\ \cos(\omega_1 t_1) & \cos(\omega_1 t_1) & \cdots & \cos(\omega_1 t_6) & \cos(\omega_1 t_6) \\ \frac{t_1}{\tau} & \frac{t_1}{\tau} & \cdots & \frac{t_6}{\tau} & \frac{t_6}{\tau} \\ \frac{\tau}{t_1} & \frac{\tau}{t_1} & \cdots & \frac{\tau}{t_6} & \frac{\tau}{t_6} \\ \frac{\tau}{t_1} & \frac{\tau}{t_1} & \cdots & \frac{\tau}{t_6} & \frac{\tau}{t_6} \\ \tau & \tau & \cdots & \tau & \tau \end{pmatrix} \quad (24)$$

$$\mathbf{L} = \begin{pmatrix} -\sin(\theta_{t_1}) \cos(\varphi_{t_1}) & \cos(\varphi_{t_1}) & \cdots & -\sin(\theta_{t_6}) \cos(\varphi_{t_6}) & \cos(\varphi_{t_6}) \\ \sin(\theta_{t_1}) \sin(\varphi_{t_1}) & \sin(\varphi_{t_1}) & \cdots & \sin(\theta_{t_6}) \sin(\varphi_{t_6}) & \sin(\varphi_{t_6}) \\ \cos(\theta_{t_1}) & 0 & \cdots & \cos(\theta_{t_6}) & 0 \\ -\sin(\theta_{t_1}) \cos(\varphi_{t_1}) & \cos(\varphi_{t_1}) & \cdots & -\sin(\theta_{t_6}) \cos(\varphi_{t_6}) & \cos(\varphi_{t_6}) \\ \sin(\theta_{t_1}) \sin(\varphi_{t_1}) & \sin(\varphi_{t_1}) & \cdots & \sin(\theta_{t_6}) \sin(\varphi_{t_6}) & \sin(\varphi_{t_6}) \\ \cos(\theta_{t_1}) & 0 & \cdots & \cos(\theta_{t_6}) & 0 \\ -\sin(\theta_{t_1}) \cos(\varphi_{t_1}) & \cos(\varphi_{t_1}) & \cdots & -\sin(\theta_{t_6}) \cos(\varphi_{t_6}) & \cos(\varphi_{t_6}) \\ \sin(\theta_{t_1}) \sin(\varphi_{t_1}) & \sin(\varphi_{t_1}) & \cdots & \sin(\theta_{t_6}) \sin(\varphi_{t_6}) & \sin(\varphi_{t_6}) \\ \cos(\theta_{t_1}) & 0 & \cdots & \cos(\theta_{t_6}) & 0 \end{pmatrix} \quad (25)$$

$$\mathbf{\Psi} = \begin{pmatrix} 1 & 1 & 0 & 0 & -1 & -1 & 0 & 0 & 0 & 0 & 0 & 0 \\ 0 & 0 & 1 & 1 & 0 & 0 & -1 & -1 & 0 & 0 & 0 & 0 \\ 0 & 0 & 0 & 0 & 1 & 1 & 0 & 0 & -1 & -1 & 0 & 0 \\ 0 & 0 & 0 & 0 & 0 & 0 & 1 & 1 & 0 & 0 & -1 & -1 \end{pmatrix} \quad (26)$$

ments that greatly helped to improve the manuscript. Any use of trade, product, or firm names is for descriptive purposes only and does not imply endorsement by the U.S. Government.

REFERENCES

- [1] R. M. Goldstein, H. Engelhardt, B. Kamb, and R. M. Frolich, "Satellite radar interferometry for monitoring ice sheet motion: Application to an antarctic ice stream," *Science*, vol. 262, no. 5139, pp. 1525–1530, 1993.
- [2] M. Simons and P. A. Rosen, "Interferometric synthetic aperture radar geodesy," in *Treatise Geophysics*, G. Schubert, Ed. Amsterdam, The Netherlands: Elsevier, 2015, pp. 339–385.
- [3] R. Bamler, "Interferometric stereo radargrammetry: Absolute height determination from ERS-ENVISAT interferograms," in *Proc. IEEE Int. Geosci. Remote Sens. Symp. (IGARSS)*, vol. 2, Jul. 2000, pp. 742–745.
- [4] A. Ferretti, C. Prati, and F. Rocca, "Permanent scatterers in SAR interferometry," *IEEE Trans. Geosci. Remote Sens.*, vol. 39, no. 1, pp. 8–20, Jan. 2001.
- [5] P. Berardino, G. Fornaro, R. Lanari, and E. Sansosti, "A new algorithm for surface deformation monitoring based on small baseline differential SAR interferograms," *IEEE Trans. Geosci. Remote Sens.*, vol. 40, no. 11, pp. 2375–2383, Nov. 2002.
- [6] D. Perissin and T. Wang, "Repeat-pass SAR interferometry with partially coherent targets," *IEEE Trans. Geosci. Remote Sens.*, vol. 50, no. 1, pp. 271–280, Jan. 2012.
- [7] E. A. Hetland, P. Musé, M. Simons, Y. N. Lin, P. S. Agram, and C. J. DiCaprio, "Multiscale InSAR Time Series (MInTS) analysis of surface deformation," *J. Geophys. Res., Solid Earth*, vol. 117, no. B2, 2012.
- [8] S. Samsonov and N d'Oreye, "Multidimensional time-series analysis of ground deformation from multiple InSAR data sets applied to Virunga Volcanic Province," *Geophys. J. Int.*, vol. 191, no. 3, pp. 1095–1108, 2012.
- [9] J. Hu *et al.*, "A Kalman filter based MTInSAR methodology for deriving 3D surface displacement evolutions," in *Proc. Fringe*, vol. 697, 2011, p. 79.
- [10] I. R. Joughin, R. Kwok, and M. A. Fahnestock, "Interferometric estimation of three-dimensional ice-flow using ascending and descending passes," *IEEE Trans. Geosci. Remote Sens.*, vol. 36, no. 1, pp. 25–37, Jan. 1998.
- [11] I. Joughin, "Ice-sheet velocity mapping: A combined interferometric and speckle-tracking approach," *Ann. Glaciol.*, vol. 34, no. 1, pp. 195–201, 2002.
- [12] E. Rignot, J. Mouginot, and B. Scheuchl, "Ice flow of the Antarctic ice sheet," *Science*, vol. 333, no. 6048, pp. 1427–1430, 2011.
- [13] V. Kumar, G. Venkataramana, and K. A. Høgda, "Glacier surface velocity estimation using SAR interferometry technique applying ascending and descending passes in Himalayas," *Int. J. Appl. Earth Observ. Geoinf.*, vol. 13, no. 4, pp. 545–551, 2011.
- [14] N. Gourmelen *et al.*, "Ice velocity determined using conventional and multiple-aperture InSAR," *Earth Planetary Sci. Lett.*, vol. 307, pp. 156–160, Jul. 2011.
- [15] T. Nagler *et al.*, "Retrieval of 3D-glacier movement by high resolution X-band SAR data," in *Proc. IEEE Int. Geosci. Remote Sens. Symp. (IGARSS)*, Jul. 2012, pp. 3233–3236.
- [16] J. Neelmeijer, M. Motagh, and H. U. Wetzel, "Estimating spatial and temporal variability in surface kinematics of the inylchek glacier, central asia, using TerraSAR-X data," *Remote Sens.*, vol. 6, no. 10, pp. 9239–9259, 2014.
- [17] B. Minchew, M. Simons, S. Hensley, H. Björnsson, F. Pálsson, and P. Milillo, "Multiple glacier surges observed with airborne and spaceborne interferometric synthetic aperture radar," in *Proc. IEEE Int. Geosci. Remote Sens. Symp. (IGARSS)*, Jul. 2015, pp. 5316–5319.
- [18] B. Minchew, M. Simons, S. Hensley, H. Björnsson, and F. Pálsson, "Early melt season velocity fields of Langjökull and Hofsjökull, central Iceland," *J. Glaciol.*, vol. 61, no. 226, pp. 253–266, 2015.
- [19] Y. Fialko, D. Sandwell, M. Simons, and P. Rosen, "Three-dimensional deformation caused by the Bam, Iran, earthquake and the origin of shallow slip deficit," *Nature*, vol. 435, no. 7040, pp. 295–299, 2005.
- [20] H. S. Jung, Z. Lu, J. S. Won, M. P. Poland, and A. Miklius, "Mapping three-dimensional surface deformation by combining multiple-aperture interferometry and conventional interferometry: Application to the June 2007 Eruption of Kilauea Volcano, Hawaii," *IEEE Geosci. Remote Sens. Lett.*, vol. 8, no. 1, pp. 34–38, Jan. 2011.
- [21] A. Manconi *et al.*, "Brief communication: Rapid mapping of landslide events: The 3 December 2013 Montescaglioso landslide, Italy," *Natural Hazards Earth Syst. Sci.*, vol. 14, no. 7, pp. 1835–1841, 2014.
- [22] F. Raspini *et al.*, "Exploitation of amplitude and phase of satellite SAR images for landslide mapping: The case of montescaglioso (South Italy)," *Remote Sens.*, vol. 7, no. 11, pp. 14576–14596, 2015.
- [23] P. Milillo *et al.*, "Monitoring dam structural health from space: Insights from novel InSAR techniques and multi-parametric modeling applied to the Pertusillo dam Basilicata, Italy," *Int. J. Appl. Earth Observ. Geoinf.*, vol. 52, pp. 221–229, Oct. 2016.
- [24] Y. Fialko, M. Simons, and D. Agnew, "The complete (3-D) surface displacement field in the epicentral area of the 1999 M_W 7.1 Hector Mine Earthquake, California, from space geodetic observations," *Geophys. Res. Lett.*, vol. 28, no. 16, pp. 3063–3066, 2001.
- [25] P. Milillo *et al.*, "Space geodetic monitoring of engineered structures: The ongoing destabilization of the Mosul dam, Iraq," *Sci. Rep.*, vol. 6, Dec. 2016, Art. no. 37408, doi: 10.1038/srep37408.
- [26] F. Casu and A. Manconi, "Four-dimensional surface evolution of active rifting from spaceborne SAR data," *Geosphere*, vol. 12, no. 3, pp. 697–705, 2016.
- [27] A. Pepe, G. Solaro, and C. Dema, "A minimum curvature combination method for the generation of multi-platform DInSAR deformation time-series," in *Proc. Adv. Sci. Appl. SAR Interferometry Sentinel-1 InSAR Workshop*, Frascati, Italy, 2015, pp. 23–27, doi: 10.5270/Fringe2015.150.
- [28] E. Rignot, J. Mouginot, and B. Scheuchl, "Antarctic grounding line mapping from differential satellite radar interferometry," *Geophys. Res. Lett.*, vol. 38, no. 10, 2011.
- [29] G. H. Gudmundsson, "Fortnightly variations in the flow velocity of Rutford Ice Stream, West Antarctica," *Nature*, vol. 444, no. 7122, pp. 1063–1064, 2006.

- [30] T. Murray, A. M. Smith, M. A. King, and G. P. Weedon, "Ice flow modulated by tides at up to annual periods at Rutford Ice Stream, West Antarctica," *Geophys. Res. Lett.*, vol. 34, no. 18, 2007.
- [31] J. Weertman, "On the sliding of glaciers," *J. Glaciol.*, vol. 3, no. 21, pp. 33–38, 1957.
- [32] J. Thompson, M. Simons, and V. C. Tsai, "Modeling the elastic transmission of tidal stresses to great distances inland in channelized ice streams," *Cryosphere*, vol. 8, no. 6, pp. 2007–2029, 2014.
- [33] P. Milillo, E. J. Fielding, W. H. Shulz, B. Delbridge, and R. Burgmann, "COSMO-SkyMed spotlight interferometry over rural areas: The Slumgullion landslide in Colorado, USA," *IEEE J. Sel. Topics Appl. Earth Observ. Remote Sens.*, vol. 7, no. 7, pp. 2919–2926, Jul. 2014.
- [34] F. Casu, A. Manconi, A. Pepe, and R. Lanari, "Deformation time-series generation in areas characterized by large displacement dynamics: The SAR amplitude pixel-offset SBAS technique," *IEEE Trans. Geosci. Remote Sens.*, vol. 49, no. 7, pp. 2752–2763, Jul. 2011.
- [35] T. Strozzi, A. Luckman, T. Murray, U. Wegmüller, and C. L. Werner, "Glacier motion estimation using SAR offset-tracking procedures," *IEEE Trans. Geosci. Remote Sens.*, vol. 40, no. 11, pp. 2384–2391, Nov. 2002.
- [36] P. A. Rosen, E. Gurrola, G. F. Sacco, and H. Zebker, "The InSAR scientific computing environment," in *Proc. 9th Eur. Conf. Synth. Aperture Radar (EUSAR)*, Apr. 2012, pp. 730–733.
- [37] P. Fretwell *et al.*, "Bedmap2: Improved ice bed, surface and thickness datasets for Antarctica," *Cryosphere*, vol. 7, no. 1, pp. 375–393, 2013.
- [38] *CSK Handbook Products—eGeos*, accessed on May 15, 2016. [Online]. Available: <http://www.e-geos.it/products/pdf/csk-product%20handbook.pdf>
- [39] B. Minchew, M. Simons, B. Riel, and P. Milillo, "Tidally induced variations in vertical and horizontal motion on Rutford Ice Stream, West Antarctica, inferred from remotely sensed observations," *J. Geophys. Res., Earth Surface*, vol. 122, no. 1, pp. 167–190, 2017.
- [40] G. H. Gudmundsson, "Tides and the flow of Rutford ice stream, West Antarctica," *J. Geophys. Res., Earth Surface*, vol. 112, no. F4, 2007.
- [41] D. Ascher, P. F. Dubois, K. Hinsien, J. Hugunin, and T. Oliphant, *Numerical Python*. 2001.



Brent Minchew received the B.S. and M.S. degrees in aerospace engineering from the University of Texas at Austin, Austin, TX, USA, in 2008 and 2010, respectively, and the Ph.D. degree in geophysics from the California Institute of Technology, Pasadena, CA, USA, in 2016.

He is currently an NSF Earth Sciences Post-Doctoral Fellow with the British Antarctic Survey, Cambridge, U.K., where he is involved in glacier dynamics, with an emphasis on remote sensing applications.



Mark Simons received the B.Sc. degree from the University of California, Los Angeles, CA, USA, in 1989, and the Ph.D. degree from the Massachusetts Institute of Technology, Cambridge, MA, USA, in 1996.

He is currently a Professor of Geophysics with the Seismological Laboratory, Division of Geological and Planetary Sciences, California Institute of Technology, Pasadena, CA, USA.

Piyush Agram, photograph and biography not available at the time of publication.



Pietro Milillo (SM'12) received the B.Sc. degree in physics and the M.Sc. degree in applied physics from the University of Bari, Bari, Italy, in 2010 and 2012, respectively, and the Ph.D. degree in environmental engineering from the University of Basilicata, Potenza, Italy, with a thesis on the synergistic use of synthetic aperture radar (SAR) constellations for studying natural and anthropogenic phenomena.

From 2013 to 2015, he was a Visiting Student with the Seismological Laboratory and a Visiting Student Researcher with the Earth Science and Technology

Division, California Institute of Technology, Pasadena, CA, USA. In 2016, he joined the Jet Propulsion Laboratory, Radar Science and Engineering Section, California Institute of Technology. His research interests include SAR applications, interferometric SAR, multitemporal analysis, cryosphere, natural hazards, and earth science.



Bryan Riel received the B.Sc. and M.Sc. degrees in aerospace engineering from the University of Texas at Austin, Austin, TX, USA, and the M.Sc. and Ph.D. degrees in geophysics from the California Institute of Technology, Pasadena, CA, USA, where he studied inverse theory and time-series analysis of GPS and interferometric synthetic aperture radar (SAR) data to characterize time-dependent ground deformation.

He was involved in the radiometric calibration of SAR and the quantification of elevation errors in backscatter products. Since 2016, he has been a Radar Scientist with the NASA's Jet Propulsion Laboratory, Pasadena, CA, USA.

Dr. Riel received the NASA Earth and Space Sciences Fellowship in 2012.